

Received October 2, 2020, accepted October 12, 2020, date of publication October 14, 2020, date of current version October 26, 2020.

Digital Object Identifier 10.1109/ACCESS.2020.3030996

Phase Noise Effect on Millimeter-Wave Pre-5G Systems

JONGHO OH¹, (Member, IEEE), AND TAE-KYOUNG KIM², (Member, IEEE)

¹Networks Business, Samsung Electronics Company Ltd., Suwon 16677, South Korea

²Department of Electronics, Information and Communication Engineering, Mokpo National University, Muan 58554, South Korea

Corresponding author: Tae-Kyoung Kim (tk415kim@gmail.com)

This work was supported by the National Research Foundation of Korea (NRF) Grant funded by the Korean Government (MIST) under Grant 2019R1G1A1007205.

ABSTRACT The introduction of millimeter waves for 5G wireless communication systems enables the use of more bandwidth and higher carrier frequency, surpassing the capacity of current systems by more than one order of magnitude. The leap of millimeter band results from the development of analog frontends that unfortunately induce relatively large phase noise in phase-locked loop synthesizers. Large phase noise may generate considerable random phase error and residual frequency offset, which in turn produces additional phase error. We evaluate phase error from phase noise on an implemented pre-5G system operating in the millimeter band and through a simulation by modeling the characteristics of a radio frequency integrated circuit. We measure and then compare the residual frequency offset, phase error, and error vector magnitude between the experimental and simulation results. We verify that the phase noise model suitably approximates to the real conditions. Moreover, we show that phase error remains at approximately 4° in the implemented system. By exploiting the implemented phase error compensation, our pre-5G system can overcome a degradation of 1.5 dB in error vector magnitude and achieve an approximate transmission rate of 4 Gbps at gain of 1.49.

INDEX TERMS 5G, millimeter-wave (mm-wave), 28GHz, phase noise (PN), carrier frequency offset, implementation.


I. INTRODUCTION

The recent introduction of millimeter waves supporting gigabit-per-second data transmission has attracted much attention regarding the development of 5G wireless communication systems [1]–[5], which are mainly adopting operation at these frequency bands. For instance, Korean Telecom developed a standard for 5G services employed during the PyeongChang 2018 Olympic Winter Games [6]. Verizon has released a pre-5G specification to occupy this new market in advance through commercial fixed wireless access in 2018 [7]. Both of these pre-5G specifications use 28 GHz as the operating band. Similarly, the 5G New Radio specification from the 3GPP (3rd Generation Partnership Project) was designed to operate in bands 26.5 – 29.5, 24.25 – 27.5, and 37 – 40 GHz [8].

Nevertheless, the use of the millimeter bands for 5G wireless communication systems still faces many technical challenges [9], [10]. For example, integrated circuits and system design are susceptible to nonlinear distortion of power

amplifiers, in-phase and quadrature imbalance, highly directional antenna design, and phase noise (PN). Specifically, severe PN is caused by the phase-locked loop synthesizers with high carrier frequency compared to the orthogonal frequency-division multiplexing (OFDM) of current cellular systems [11], [12]. PN on OFDM has been studied mainly to mitigate the common phase error (CPE) by compensating a constant phase error among sub-carriers in an OFDM symbol [13]–[15]. The CPE is usually estimated by using least square [13], [14] or minimum mean square error estimation [15] from dedicated reference signals (RSs). Achievable rate in the CPE channels was investigated in [16]. Based on the CPE, inter-carrier interference can be also suppressed by non-iterative [17], [18] and iterative [19] methods. For the non-iterative method, suppression based on the cyclic prefix and minimum mean square error have been introduced in [17] and [18], respectively, whereas for the iterative method, joint PN compensation and channel estimation has been considered [19].

Various studies have been focused on PN compensation to mitigate the CPE and inter-carrier interference by considering only random phase errors. However, in real settings,

The associate editor coordinating the review of this manuscript and approving it for publication was Rocco Giofrè .

considerable PN may generate estimation error of the carrier frequency offset, reflecting residual frequency offset (RFO). As RFO is more severe in the millimeter bands [20], the PN and RFO effects should be jointly investigated. In [14], [21], PN and carrier frequency offset have been considered for their estimation and compensation, but neglecting the RFO effect. In addition, the phase error caused by PN has not been well addressed in 5G communication systems based on the millimeter band. Although PN has been successfully mitigated in millimeter bands by using least squares and least mean squares methods [22]–[24], RFO has not been considered despite of its importance in these bands.

In this article, we analyze the PN effect on a pre-5G system operating in millimeter bands. We first formulate the OFDM signal model and PN model considering both PN and RFO. We also introduce our system based on the pre-5G specification [7] and describe its implementation as user equipment for fixed wireless access systems. To analyze the PN effect on the implemented pre-5G system, we discuss the method and implementation of phase error compensation using an RS for PN. Next, by applying the characteristics of the implemented pre-5G system to the system model, the PN effect on the system is evaluated via simulations. We confirm that the RFO should be reduced given the accumulation at the initial frequency estimation, because the PN influence on the RFO is substantial. After a reasonable accumulation, we observe that the phase error remains at approximately 4° , as confirmed by the results showing similar simulated and measured phase errors. Finally, by exploiting the implemented phase error compensation, we confirm that the error vector magnitude (EVM) and throughput of the pre-5G system are over 1.5 dB and 1.49 times gain compared to those before compensation, respectively. Our key contributions are summarized as follows.

- Based on the pre-5G specification, we describe the hardware implementation of our system, which uses one radio frequency unit to support multiple component carriers. Thus, the sampling rate of the radio frequency unit is oversampled by the number of multiple component carriers, and the oversampled signal is digitally divided to perform a modem operation per component carrier. In this structure, we introduce a phase error compensator and its implementation. In addition, the phase error effect is investigated in the pre-5G system using millimeter bands, possibly establishing a performance indicator for next-generation millimeter-wave systems.
- We investigate the PN effects on the implemented system. PN generates RFO despite sufficient accumulation at the initial carrier-frequency offset estimation, which is approximately 72 Hz. As this amount is non-negligible, the phase error is not completely mitigated by the compensator. The EVM and throughput are degraded by 1.5 dB and 149% at 28 dB, respectively, without using phase error compensation.
- To quantify the PN effect, we introduce random phase error and RFO in the OFDM system model, from which

we simulate the phase error compensator using the pre-5G system parameters. We consider the OFDM system model based on a partially-connected hybrid architecture with dual-polarization. The performance of the PN effect on a fully-connected hybrid architecture was investigated in [25]. In contrast to [25], we employ a partially-connected architecture in which each RF chain is connected to its own antenna elements. In this architecture, the PN can be effectively mitigated when it is assumed to be a common PN [26]. Compared to [26], we further extend the system model to an independent PN and to a dual-polarized antenna. In addition, the PN effect is evaluated based on the extended system model and is compared between the simulated and implemented compensators. The simulated phase error well approximates the experimental phase error. This approximation shows that the PN effect on the implemented system is interpreted from two RF impairments of a random phase error and RFO.

The general background of this study and an overview of related studies have been presented in this section. The system model assumed for this study is described in Section II. The pre-5G specification and phase error compensation are detailed in Section III. The implementation of the pre-5G system is provided in Section IV. The analyses of PN effect on phase error and system performance are reported in Section V, where simulation and experimental results are also provided. Finally, conclusions are drawn in Section VI.

Notation: Superscripts $(\cdot)^H$ and $(\cdot)^*$ denote the conjugate transpose and conjugate operation, respectively. $|\cdot|$ denotes the cardinality of a set. The set \mathbb{C} represents the set of complex numbers. Functions $\arg\{\cdot\}$, $\text{diag}(\cdot)$, and $\text{blkdiag}(\cdot)$ are the phase operation, diagonal operation for a vector, and block diagonal operation for vectors, respectively. Notations \mathbf{X}_{ab} and \mathbf{x}_a are the (a, b) -th entry of a matrix \mathbf{X} and a -th entry of a vector \mathbf{x} , respectively. Notations \circ , \otimes , and \circledast are the Hadamard product, Kronecker product, and circular convolution, respectively.

II. SYSTEM MODEL

We first model a dual-polarization multi-input, multi-output (MIMO) channel for 5G wireless communication systems. Next, we introduce the system model that well approximates the characteristics in millimeter bands. From the system model, we qualitatively analyze the PN effect by introducing random phase error and RFO. These models are utilized to quantitatively evaluate the system performance at the Section V.

A. CHANNEL MODEL

A millimeter MIMO system with dual polarization uniform planner arrays (UPAs) is considered where a transmitter with N_t^c RF chains serves a receiver with N_r^c RF chains (see Fig. 1). RF chains are partially connected to a phase shifter that adjusts analog beamforming using antenna elements [27]. The numbers of antenna elements per RF chain

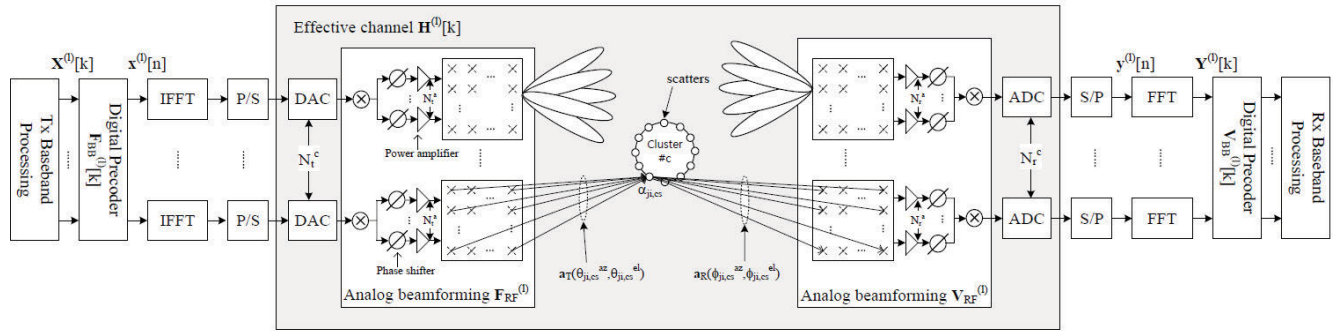


FIGURE 1. A millimeter-wave MIMO-OFDM system with a partially-connected hybrid beamforming structure.

at the transmitter and receiver are $N_t^a = 2N_{t,h} \times N_{t,v}$ and $N_r^a = 2N_{r,h} \times N_{r,v}$, respectively. The subscript v and h represent vertical and horizontal placement, respectively. Thus, the total numbers of antenna elements at the transmitter and receiver are $N_t = N_t^a N_t^c$ and $N_r = N_r^a N_r^c$, respectively.

A millimeter-wave channel that consists of a line-of-sight (LOS) path and N_{cl} non-line-of-sight (NLOS) paths is adopted where N_{cl} is the number of clusters [25]. Thereafter, the channel between the i -th transmitter and j -th receiver RF chains at time n for OFDM symbol l is defined as follows:

$$\mathbf{g}_{ji}^{(l)}[n] = \sqrt{\frac{K}{K+1}} \mathbf{g}_{ji,L}^{(l)}[n] + \sqrt{\frac{1}{K+1}} \mathbf{g}_{ji,S}^{(l)}[n], \quad (1)$$

where the parameter K is the Rician K -factor. The matrices $\mathbf{g}_{ji,L}^{(l)}[n] \in \mathbb{C}^{N_r^a \times N_t^a}$ and $\mathbf{g}_{ji,S}^{(l)}[n] \in \mathbb{C}^{N_r^a \times N_t^a}$ are the channels of LOS path and NLOS paths, respectively. For dual-polarization UPA [28], they are, respectively, determined as follows:

$$\begin{aligned} & \mathbf{g}_{ji,L}^{(l)}[n] \\ &= \sqrt{\frac{N_r^a N_t^a}{2^2}} \alpha_{ji,L} \left\{ \begin{pmatrix} \sqrt{\frac{1}{1+\chi}} & \sqrt{\frac{\chi}{1+\chi}} \\ \sqrt{\frac{\chi}{1+\chi}} & \sqrt{\frac{1}{1+\chi}} \end{pmatrix} \right. \\ & \quad \circ \begin{bmatrix} e^{j\xi_{ji,L}^{vv}} & e^{j\xi_{ji,L}^{vh}} \\ e^{j\xi_{ji,L}^{hv}} & e^{j\xi_{ji,L}^{hh}} \end{bmatrix} \otimes \left(\mathbf{a}_R(\phi_{ji,L}^{az}, \phi_{ji,L}^{el}) \mathbf{a}_T^H(\theta_{ji,L}^{az}, \theta_{ji,L}^{el}) \right) \left. \right\}, \\ & \mathbf{g}_{ji,S}^{(l)}[n] \\ &= \sqrt{\frac{N_r^a N_t^a}{2^2} \sum_{c=1}^{N_{cl}} \sum_{s=1}^{N_{p,c}} \alpha_{ji,cs}} \left\{ \begin{pmatrix} \sqrt{\frac{1}{1+\chi}} & \sqrt{\frac{\chi}{1+\chi}} \\ \sqrt{\frac{\chi}{1+\chi}} & \sqrt{\frac{1}{1+\chi}} \end{pmatrix} \right. \\ & \quad \circ \begin{bmatrix} e^{j\xi_{ji,cs}^{vv}} & e^{j\xi_{ji,cs}^{vh}} \\ e^{j\xi_{ji,cs}^{hv}} & e^{j\xi_{ji,cs}^{hh}} \end{bmatrix} \otimes \left(\mathbf{a}_R(\phi_{ji,cs}^{az}, \phi_{ji,cs}^{el}) \mathbf{a}_T^H(\theta_{ji,cs}^{az}, \theta_{ji,cs}^{el}) \right) \left. \right\}, \end{aligned} \quad (2)$$

where the channel gains of LOS path and the s -th path corresponding to the c -th cluster between the i -th transmitter and j -th receiver RF chains are defined as $\alpha_{ji,L}$ and $\alpha_{ji,cs}$, respectively. The number of paths for the c -th cluster denotes $N_{p,c}$. The inverse of cross-polar discrimination (XPD) is χ .

A random phase $\xi_{ji,p}^{ab}$ is uniformly distributed in $[0, 2\pi]$ where $p \in \{L, 11, \dots, N_{cl} N_{p,N_{cl}}\}$, $a \in \{v, h\}$ and $b \in \{v, h\}$. The array response vector for angle-of-departure (AoD) with azimuth and elevation $(\theta_{ji,p}^{az}, \theta_{ji,p}^{el})$ is determined as follows: $\mathbf{a}_T(\theta_{ji,p}^{az}, \theta_{ji,p}^{el}) \in \mathbb{C}^{\frac{N_t^a}{2} \times 1}$. Similarly, the array response vector for angle-of-arrival (AoA) with azimuth and elevation $(\phi_{ji,p}^{az}, \phi_{ji,p}^{el})$ is determined as follows: $\mathbf{a}_R(\phi_{ji,p}^{az}, \phi_{ji,p}^{el}) \in \mathbb{C}^{\frac{N_r^a}{2} \times 1}$. The array response vector of p -th path for the i -th transmit RF chain is

$$\mathbf{a}_T(\theta_{ji,p}^{az}, \theta_{ji,p}^{el}) = \mathbf{a}_{T,h}(\theta_{ji,p}^{az}, \theta_{ji,p}^{el}) \otimes \mathbf{a}_{T,v}(\theta_{ji,p}^{el}), \quad (3)$$

where the array response vectors of horizontally and vertically arranged uniform linear arrays (ULAs) are $\mathbf{a}_{T,h}(\theta_{ji,p}^{az}, \theta_{ji,p}^{el}) \in \mathbb{C}^{N_{t,h} \times 1}$ and $\mathbf{a}_{T,v}(\theta_{ji,p}^{el}) \in \mathbb{C}^{N_{t,v} \times 1}$, respectively. They are determined as follows:

$$\begin{aligned} \mathbf{a}_{T,h}(\theta_{ji,p}^{az}, \theta_{ji,p}^{el}) &= \frac{1}{\sqrt{N_{t,h}}} \left[1, e^{\frac{j2\pi d_{t,h}}{\lambda} \sin(\theta_{ji,p}^{az}) \cos(\theta_{ji,p}^{el})}, \dots, \right. \\ & \quad \left. e^{\frac{j2\pi d_{t,h}}{\lambda} (N_{t,h}-1) \sin(\theta_{ji,p}^{az}) \cos(\theta_{ji,p}^{el})} \right]^T, \\ \mathbf{a}_{T,v}(\theta_{ji,p}^{el}) &= \frac{1}{\sqrt{N_{t,v}}} \left[1, e^{\frac{j2\pi d_{t,v}}{\lambda} \sin(\theta_{ji,p}^{el})}, \dots, \right. \\ & \quad \left. e^{\frac{j2\pi d_{t,v}}{\lambda} (N_{t,v}-1) \sin(\theta_{ji,p}^{el})} \right]^T, \end{aligned} \quad (4)$$

where the wavelength denotes λ . The intervals of the horizontal and vertical ULAs are $d_{t,h}$ and $d_{t,v}$, respectively. Similar to $\mathbf{a}_{T,h}(\theta_{ji,p}^{az}, \theta_{ji,p}^{el})$, we can obtain the array response vector $\mathbf{a}_R(\phi_{ji,p}^{az}, \phi_{ji,p}^{el})$ for the j -th receive RF chain.

In practical, the system performance depends on an effective channel that contains analog beamformings [29], [30]. Let the analog beamformings for OFDM symbol l at the transmitter and receiver be $\mathbf{F}_{RF}^{(l)} \in \mathbb{C}^{N_t \times N_t^c}$ and $\mathbf{V}_{RF}^{(l)} \in \mathbb{C}^{N_r \times N_r^c}$, respectively. They are, respectively, expressed as follows:

$$\begin{aligned} \mathbf{F}_{RF}^{(l)} &= \text{blkdiag} \left(\mathbf{F}_{1,RF}^{(l)}, \dots, \mathbf{F}_{N_r^c,RF}^{(l)} \right), \\ \mathbf{V}_{RF}^{(l)} &= \text{blkdiag} \left(\mathbf{V}_{1,RF}^{(l)}, \dots, \mathbf{V}_{N_r^c,RF}^{(l)} \right), \end{aligned} \quad (5)$$

where the analog beamforming vectors for the i -th transmitter and for the j -th receiver RF chains are defined as $\mathbf{F}_{i,RF}^{(l)} \in \mathbb{C}^{N_t^a \times 1}$ and $\mathbf{V}_{j,RF}^{(l)} \in \mathbb{C}^{N_r^a \times 1}$, respectively. Using (5), the effective channel $\mathbf{h}^{(l)}[n] \in \mathbb{C}^{N_r^c \times N_t^c}$ at time n for the OFDM symbol l is expressed as follows:

$$\mathbf{h}^{(l)}[n] = (\mathbf{V}_{RF}^{(l)})^H \mathbf{g}^{(l)}[n] \mathbf{F}_{RF}^{(l)}, \quad (6)$$

where $n = 0, 1, \dots, L - 1$ where the delay spread denotes L . The channel matrix $\mathbf{g}^{(l)}[n] \in \mathbb{C}^{N_r^c \times N_t^c}$ can be obtained from (1) as follows:

$$\mathbf{g}^{(l)}[n] = \begin{bmatrix} \mathbf{g}_{11}^{(l)}[n] & \dots & \mathbf{g}_{1N_t^c}^{(l)}[n] \\ \vdots & \ddots & \vdots \\ \mathbf{g}_{N_r^c 1}^{(l)}[n] & \dots & \mathbf{g}_{N_r^c N_t^c}^{(l)}[n] \end{bmatrix}. \quad (7)$$

We use the effective channel model in (6) to the system model because the system performance can be characterized by the effective channel.

B. SIGNAL MODEL

We consider a subframe-based MIMO-OFDM system with N_{sym} OFDM symbols. The n -th sample $\mathbf{x}^{(l)}[n] \in \mathbb{C}^{N_t^c \times 1}$ for OFDM symbol l in a subframe is described as follows:

$$\mathbf{x}^{(l)}[n] = \frac{1}{\sqrt{N}} \sum_{k=0}^{N-1} \mathbf{F}_{BB}^{(l)}[k] \mathbf{X}^{(l)}[k] e^{j2\pi(k - \frac{N}{2})\frac{(n-c_l)}{N}}, \quad (8)$$

where $n = 0, 1, \dots, (c_l + N - 1)$. The number of samples for cyclic prefix in the OFDM symbol l denotes c_l where $l = 0, 1, \dots, N_{sym} - 1$. When the sub-carrier spacing and number of time units are Δf and T_s , respectively, the fast Fourier transform (FFT) size N is defined as $1/(\Delta f T_s)$. A digital precoding for the k -th sub-carrier of the OFDM symbol l at the transmitter is given by $\mathbf{F}_{BB}^{(l)}[k] \in \mathbb{C}^{N_t^c \times N_s^c}$, where the number of data streams N_s is assumed that $N_s = \min(N_t^c, N_r^c)$. The frequency-domain sub-carrier denotes $\mathbf{X}^{(l)}[k] \in \mathbb{C}^{N_s^c \times 1}$. M adjacent sub-carriers $\{\mathbf{X}^{(l)}[k]\}_{k=N/2-M/2}^{N/2+M/2-1}$ are assigned to modulated symbols, and zero sub-carriers are inserted into the $N - M$ unused sub-carriers. Among the M sub-carriers, RS sub-carriers $\{\mathbf{X}^{(l)}[k]\}_{k \in \mathcal{I}_i}$ are assigned to a pre-defined location, where \mathcal{I}_i is an index set at the i -th transmitter RF chain, and the remainder are assigned as data sub-carriers.

After upconversion to carrier frequency f_c with bandwidth B , a time-continuous signal is transmitted over a channel, which is described by discrete-time impulse response $\{\mathbf{h}^{(l)}[m]\}_{m=0}^{L-1}$ in (6) with duration LT_s . Considering that PN is a multiplicative noise process, the n -th received sample $\mathbf{y}^{(l)}[n] \in \mathbb{C}^{N_r^c \times 1}$ for OFDM symbol l is determined as follows:

$$\mathbf{y}^{(l)}[n] = \boldsymbol{\psi}_R^{(l)}[n] \left(\mathbf{h}^{(l)}[n] \otimes \left(\boldsymbol{\psi}_T^{(l)}[n] \mathbf{x}^{(l)}[n] \right) \right) + \mathbf{w}^{(l)}[n]. \quad (9)$$

where the n -th PN component for the OFDM symbol l at the transmitter and receiver are defined as $\boldsymbol{\psi}_T^{(l)}[n] \in \mathbb{C}^{N_t^c \times N_t^c}$ and $\boldsymbol{\psi}_R^{(l)}[n] \in \mathbb{C}^{N_r^c \times N_r^c}$, respectively [31], [32]. They are

expressed as follows:

$$\begin{aligned} \boldsymbol{\psi}_T^{(l)}[n] &= \text{diag} \left(e^{j\omega_{T,1}^{(l)}[n]}, \dots, e^{j\omega_{T,N_t^c}^{(l)}[n]} \right), \\ \boldsymbol{\psi}_R^{(l)}[n] &= \text{diag} \left(e^{j\omega_{R,1}^{(l)}[n]}, \dots, e^{j\omega_{R,N_r^c}^{(l)}[n]} \right) e^{j2\pi\epsilon \frac{n+(N+c_l)l}{N}}, \end{aligned} \quad (10)$$

where random phase errors at the i -th transmitter and the j -th receiver RF chains are $\omega_{T,i}^{(l)}[n]$ and $\omega_{R,j}^{(l)}[n]$, respectively. $\epsilon = f_o/\Delta f$ is a normalized RFO that produces a linear phase error and its effect is discussed in Section II-C. Notably, the RFO is considered to evaluate the PN effect in a realistic scenario because carrier frequency offset estimation is imperfect in the presence of PN, and the error is non-negligible. $\mathbf{w}^{(l)}[n] \in \mathbb{C}^{N_r^c \times 1}$ in (9) is the n -th component of additive noise for the OFDM symbol l with variance W_0 .

To reflect the behavior of random phase errors $\omega_{T,i}^{(l)}[n]$ and $\omega_{R,j}^{(l)}[n]$ at millimeter bands, we exploit the PN power spectral density modeled by the three pole-zero model in [33] as follows:

$$P(f) = P(0) \left[\frac{1 + (f/f_{z_1})^2}{1 + (f/f_{p_1})^2} \right] \left[\frac{1 + (f/f_{z_2})^2}{1 + (f/f_{p_2})^2} \right] \left[\frac{1 + (f/f_{z_3})^2}{1 + (f/f_{p_3})^2} \right], \quad (11)$$

where f_{z_m} and f_{p_m} are the m -th zero and pole values, respectively, and $P(f)$ is given as power ratio of a signal to a carrier signal (in decibels) per hertz (dBc/Hz).

C. PN EFFECT

After removing the cyclic prefix samples from the received sample in (9), it is converted into the frequency domain by the N point FFT:

$$\mathbf{Y}^{(l)}[k] = \frac{1}{\sqrt{N}} \sum_{n=0}^{N-1} \mathbf{y}^{(l)}[n + c_l] e^{-j2\pi(k - \frac{N}{2})\frac{n}{N}}. \quad (12)$$

Substituting (9) into (12), we obtain the following:

$$\begin{aligned} \mathbf{Y}^{(l)}[k] &= \boldsymbol{\Psi}_R^{(l)}[k] \otimes \left(\mathbf{H}^{(l)}[k] \left(\boldsymbol{\Psi}_T^{(l)}[k] \otimes \left(\mathbf{F}_{BB}^{(l)}[k] \mathbf{X}^{(l)}[k] \right) \right) \right) + \mathbf{W}^{(l)}[k] \\ &= \sum_{m=0}^{N-1} \sum_{n=0}^{N-1} \boldsymbol{\Psi}_R^{(l)}[k - n] \mathbf{H}^{(l)}[n] \boldsymbol{\Psi}_T^{(l)}[n - m] \mathbf{F}_{BB}^{(l)}[m] \mathbf{X}^{(l)}[m] \\ &\quad + \mathbf{W}^{(l)}[k], \end{aligned} \quad (13)$$

where the N -point FFT applied the phase error matrices $\boldsymbol{\psi}_R^{(l)}[n]$ and $\boldsymbol{\psi}_T^{(l)}[n]$ for the OFDM symbol l , which are determined as follows:

$$\begin{aligned} \boldsymbol{\Psi}_R^{(l)}[k] &= \frac{1}{\sqrt{N}} \sum_{n=0}^{N-1} \boldsymbol{\psi}_R^{(l)}[n + c_l] e^{-j2\pi(k - \frac{N}{2})\frac{n}{N}}, \\ \boldsymbol{\Psi}_T^{(l)}[k] &= \frac{1}{\sqrt{N}} \sum_{n=0}^{N-1} \boldsymbol{\psi}_T^{(l)}[n + c_l] e^{-j2\pi(k - \frac{N}{2})\frac{n}{N}}. \end{aligned} \quad (14)$$

The effective channel frequency response (CFR) $\mathbf{H}^{(l)}[k] \in \mathbb{C}^{N_f \times N_f}$ is applied as follows:

$$\mathbf{H}^{(l)}[k] = \sum_{n=0}^{N-1} \mathbf{h}^{(l)}[n + c_l] e^{-j2\pi(k - \frac{N}{2})\frac{n}{N}}, \quad (15)$$

where $\{\mathbf{h}^{(l)}[m]\}_{m=L}^{N-1} = 0$. The frequency domain noise component is determined as follows:

$$\mathbf{W}^{(l)}[k] = \frac{1}{\sqrt{N}} \sum_{n=0}^{N-1} \mathbf{w}^{(l)}[n + c_l] e^{-j2\pi(k - \frac{N}{2})\frac{n}{N}}. \quad (16)$$

After re-expressing (13), we obtain the following:

$$\begin{aligned} \mathbf{Y}^{(l)}[k] &= \Psi_R^{(l)}[0] \mathbf{H}^{(l)}[k] \Psi_T^{(l)}[0] \mathbf{F}_{BB}^{(l)}[k] \mathbf{X}^{(l)}[k] \\ &+ \sum_{n \neq k} \Psi_R^{(l)}[k - n] \mathbf{H}^{(l)}[n] \Psi_T^{(l)}[n - k] \mathbf{F}_{BB}^{(l)}[k] \mathbf{X}^{(l)}[k] \\ &+ \sum_{m \neq k} \sum_{n=0}^{N-1} \Psi_R^{(l)}[k - n] \mathbf{H}^{(l)}[n] \Psi_T^{(l)}[n - m] \cdot \\ &\mathbf{F}_{BB}^{(l)}[m] \mathbf{X}^{(l)}[m] + \mathbf{W}^{(l)}[k]. \end{aligned} \quad (17)$$

The first term in (17) is further simplified as follows:

$$\left(\Psi^{(l)} \circ \mathbf{H}^{(l)}[k] \right) \mathbf{F}_{BB}^{(l)}[k] \mathbf{X}^{(l)}[k], \quad (18)$$

where a CPE matrix $\Psi^{(l)} \in \mathbb{C}^{N_f \times N_f}$ is defined as follows:

$$\Psi^{(l)} = \begin{bmatrix} \Psi_{R,1}^{(l)}[0] \Psi_{T,1}^{(l)}[0] & \dots & \Psi_{R,1}^{(l)}[0] \Psi_{T,N_f}^{(l)}[0] \\ \vdots & \ddots & \vdots \\ \Psi_{R,N_f}^{(l)}[0] \Psi_{T,1}^{(l)}[0] & \dots & \Psi_{R,N_f}^{(l)}[0] \Psi_{T,N_f}^{(l)}[0] \end{bmatrix}. \quad (19)$$

In (19), $\Psi_{R,j}^{(l)}[0]$ and $\Psi_{T,i}^{(l)}[0]$ are the scalars with the j -th and i -th diagonal elements of $\Psi_R^{(l)}[0]$ and $\Psi_T^{(l)}[0]$, respectively. We refer $\Psi^{(l)}$ as the CPE matrix because the constellation for each sub-carrier has the same rotation over an OFDM symbol, whose (j, i) -th entry is expressed from (10), (14), and (19) as

$$\Psi_{ji}^{(l)} = \frac{1}{N} \sum_{m=0}^{N-1} \sum_{n=0}^{N-1} (-1)^{m+n} e^{j(\omega_{T,i}^{(l)}[m+c_l] + \omega_{R,j}^{(l)}[n+c_l])} \cdot e^{j2\pi \frac{n+c_l+(N+c_l)l}{N}}. \quad (20)$$

In (20), the phase error consists of two terms, one random and another linear. The random phase error is averaged over the symbol, whereas the linear phase error increases with the symbol index and results from the RFO.

The second and third terms of (17) represent inter-carrier interference. Information among other sub-carriers is summed and multiplied by some function of the phase error, inter-carrier interference results in the loss of orthogonality and may degrade the system performance. In this article, we focus on the phase error rather than the inter-carrier interference, because the CPE is dominant in the system performance. In addition, as inter-carrier interference compensation is difficult to implement, we omitted by the burden on the resulting chip size.

TABLE 1. Key system parameters of pre-5G specification.

Parameter	Symbol	Value
Carrier frequency	f_c	28 GHz
Bandwidth per CC	B	100 MHz
Number of symbols	N_{sym}	14
Sub-carrier spacing	Δf	75 kHz
Effective sub-carrier size	M	1200
FFT size	N	2048
Time unit	T_s	6.5104 ns
Cyclic prefix size	c_l	160 for $l = 0, 7$; 144 for $l \neq 0, 7$

III. PRE-5G SYSTEM DESIGN

Applying key system parameters from the pre-5G specification [7] to the signal model in Section II-B, we first describe the pre-5G communication system. Then, to discuss phase error compensation, PN compensation RS (PC-RS) in the pre-5G specification is detailed. Based on PC-RS, we describe the algorithms for estimation and compensation. For estimation, we use the least squares method, from which we obtain the CPE including the random and linear phase errors. The estimated CPE is compensated in the frequency domain. Omitting domain transformation makes the algorithm efficient for implementation.

A. PRE-5G SPECIFICATION

The center carrier frequency f_c of the pre-5G system is 28 GHz. Eight component carriers (CCs) with bandwidth of 100 MHz per carrier are available at the 28 GHz band. In the CC, one radio frame consists of 50 subframes with total duration $(\Delta f N / 100) \cdot T_s = 10$ ms (i.e., 0.2 ms per subframe). Each subframe is composed of 14 consecutive OFDM symbols with duration of 14.38 and 14.28 μ s for $l = 0, 7$ and $l \neq 0, 7$, respectively. The key system parameters in the pre-5G specification are listed in Table 1.

Each symbol can be used as a physical broadcast channel (xPBCH), extended PBCH (ePBCH), physical downlink control channel (xPDCCH), and physical downlink shared channel (xPDSCH) during downlink transmission. For uplink transmission, each symbol can be used as physical uplink shared channel (xPUSCH), physical random access channel (xPRACH), and physical uplink control channel (xPUCCH). Specifically, subframes 0 and 25 are assigned as xPBCH with synchronization signal (SS) and beam RS (BRS). Subframes 4 and 15 are assigned as ePBCH and as xPRACH, respectively. In the other subframes, xPDSCH and xPUSCH can be scheduled with xPDCCH and xPUCCH for a self-contained concept, resulting in supporting dynamic time-division duplex (TDD). Transmission of xPDCCH, xPDSCH, xPUCCH, and xPUSCH can only occur at $l = 0, 1, l = 1, 2, \dots, 13, l = 13$, and $l = 2, 3, \dots, 13$, respectively.

Fig. 2 illustrates the frame structure where xPBCH is assigned 0 and 25. ePBCH and xPRACH are assigned to subframes 4 and 15, respectively, and for the remaining subframes, xPDSCHs are assigned except for subframe 33, which corresponds to xPUSCH. Using this TDD

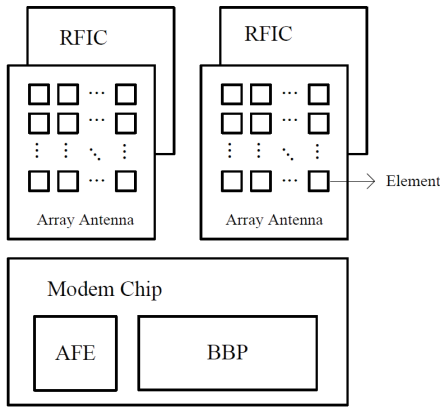


FIGURE 4. Implemented pre-5G system and corresponding block diagram.

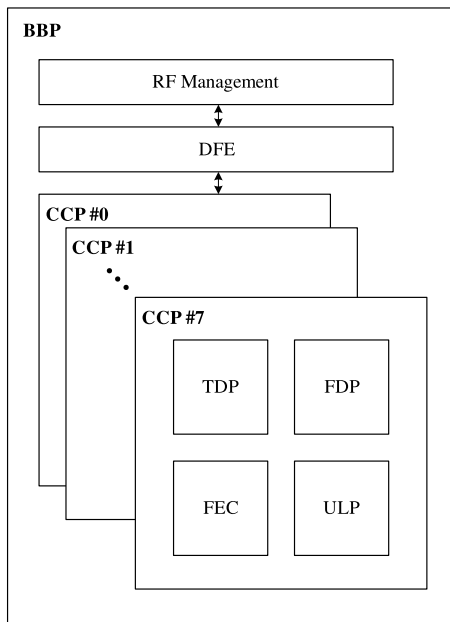


FIGURE 5. Block diagram of BBP in modem chip.

beamformings in the RFIC to obtain a sufficiently large and effective channel power. Thus, the PN effect is more pronounced by reducing the AoA/AoD mismatches. The carrier and intermediate frequencies are 28 and 1.8432 GHz, respectively. The bandwidth is 800 MHz to support the eight CCs.

The modem chip is composed of analog front-end (AFE) and baseband processor (BBP). To follow the pre-5G specification, the sampling rate per CC is required to be 153.6 MSa/s. As the implemented RFIC deals with the integrated signal for the eight CCs, the required sampling rate is 1.2288 GSa/s. In addition, we perform twofold oversampling of the integrated signal. The AFE converts between analog and digital signals, with the latter at a sampling rate of 2.4576 GSa/s. The BBP transmits/receives the digital signal to/from the AFE and is composed of RF management, digital front-end (DFE), and eight CC processors (CCPs) (see Fig. 5). In practice, the amplitude of the digital signal

at the BBP should be adjusted according to each beam. The beam and gain in the RFIC can be controlled by RF management, which is a common block given the single RFIC. Hence, the beam and gain of the eight CCs are controlled identically. Based on the beam and gain, the DFE separates the received signal from the AFE for downlink and combines the transmitted signals from the CCPs for uplink.

The separated signal is processed in the CCP, which consists of time-domain processor (TDP), frequency-domain processor (FDP), and forward error correction (FEC) for downlink transmission. In the TDP, coarse time and frequency synchronizations are performed in the SS. Then, the coarse estimates are accumulated to improve accuracy, and the accumulated estimates are compensated. A large PN introduces RFO during coarse synchronization regardless of accumulation. Thus, fine synchronization including phase error compensation should be performed in the FDP. To this end, the synchronized signal is transformed into the frequency domain by the FFT. From the synchronized frequency, the FDP performs channel estimation from the demodulation RS and phase error compensation from PC-RS. Then, for MIMO detection, log-likelihood ratios are generated for xPBCH, ePBCH, xPDCCH, and xPDSCH to perform forward error correction and decode the corresponding information bits.

For uplink transmission, xPRACH, xPUCCH, xPUSCH, and related RSs are generated in the uplink processor (ULP). The signals per CC are combined in the DFE. After adjusting the beam and gain, the combined signal is transmitted to the AFE. Finally, the combined signal in the AFE is converted into an analog signal, whose sampling rate is 2.4576 GSa/s.

B. PHASE ERROR COMPENSATION

The coarse frequency offset is compensated in the TDP by a delay correlator. However, the random phase error and RFO caused by PN may not be suitably compensated in the time domain. Hence, the phase error should be digitally compensated at the FDP. Here, we describe the implementation of phase error compensation.

Fig. 6 shows the block diagram of phase error compensation in the FDP. To estimate and compensate the phase error, sub-carrier and symbol demapper, channel estimator, and phase error compensator (PEC) are required. The compensator is in turn composed of complex multiplier, complex conjugator, PC-RS generator, coordinate rotation digital computer (CORDIC), accumulator, and phase rotator. First, the PC-RSs and demodulation RSs are demapped from the frequency-domain received signal in the sub-carrier and symbol demapper. Then, the CFRs of all sub-carriers are estimated from the demapped demodulation RSs at the channel estimator. Next, based on the received PC-RSs and estimated CFRs, estimation and compensation of phase error are performed in the PEC. In the complex multiplier, the received PC-RS, estimated CFR, and PC-RS from the corresponding generator are multiplied. After multiplication, the phase can be estimated from the CORDIC through angular operations.

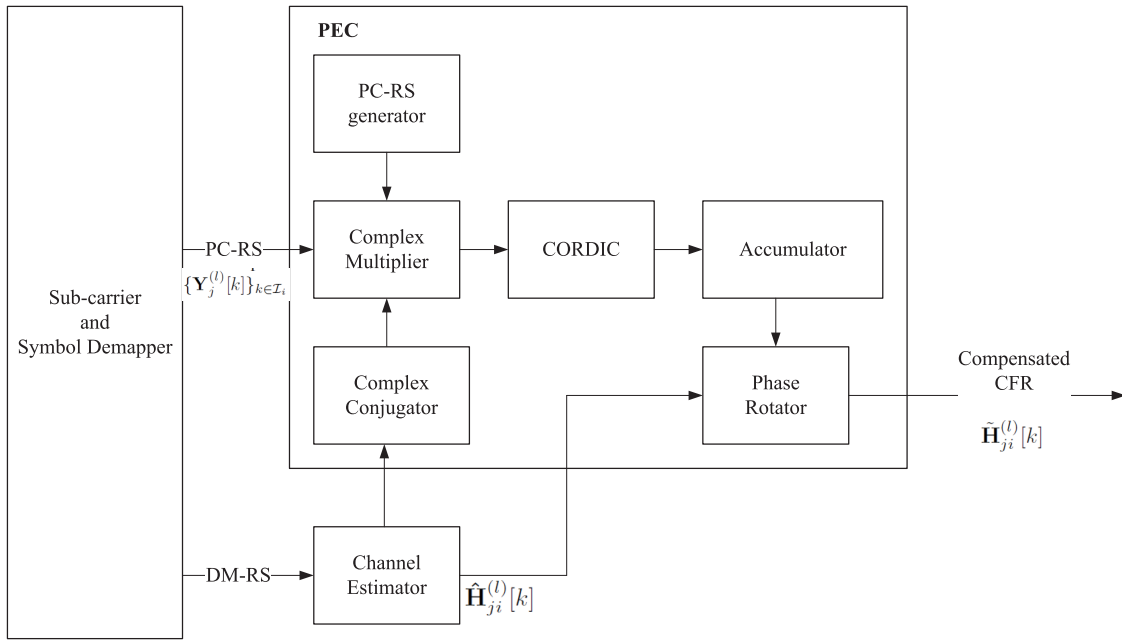


FIGURE 6. Block diagram of phase error compensation.

TABLE 2. Pole-zero values via RFIC in pre-5G system.

m	f_{p_m} [MHz]	f_{z_m} [MHz]
1	0.13	2.40
2	0.20	2.40
3	5.80	27.00

Then, the estimated phases for all PC-RS sub-carriers in the same symbol are averaged to calculate the CPE in the accumulator. Finally, the estimated CFRs for all the sub-carriers are identically rotated with the estimated CPE to obtain the compensated CFRs.

V. PERFORMANCE EVALUATION

In this section, we apply characteristics of the implemented RFIC to the system model from Section II. Then, the RFO, phase error, and EVM performance under PN are evaluated via computer simulations. In addition, the PN effect measured in the implemented pre-5G system from Section IV is evaluated for comparison with the simulation results.

A. PN EFFECT ON PRE-5G SYSTEM

We first obtain the PN model for the pre-5G system to evaluate its performance. To fit the experimental PN curve of the RFIC in the pre-5G system, the suitable values for the poles and zeroes in (11) are listed in Table 2. From these values, the PN power spectral density via RFIC in the pre-5G system is shown in Fig. 7 with an approximate value of -82 dBc/Hz for sub-carrier spacing of 75 kHz, thus being able to severely degrade the system performance.

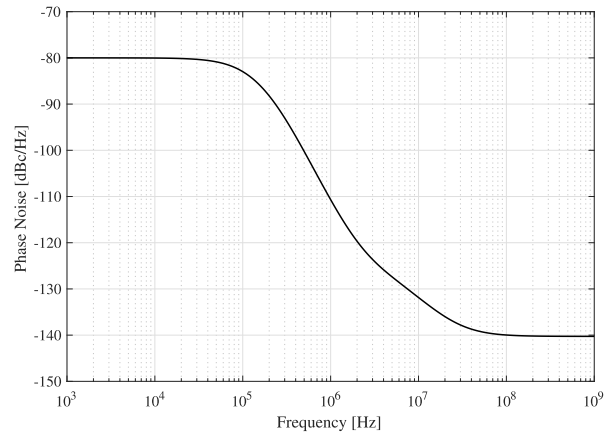


FIGURE 7. PN model for RFIC in pre-5G system.

We consider a millimeter-wave channel model in [34]. The numbers of clusters N_{cl} and paths $N_{p,c}$ are uniformly distributed in [1, 6] and [1, 30], respectively. The elevation and azimuth angles $(\theta_p^{az}, \theta_p^{el})$ for AoD and $(\phi_p^{az}, \phi_p^{el})$ for AoA are generated by using the 28 GHz LOS channel parameters specified in [34]. We set $d_{t,h} = d_{r,v} = d_{r,h} = d_{r,v} = \lambda/2$ for simplicity. Experiments on the implemented pre-5G system are conducted in a LOS dominated scenario. Corresponding to the scenario, the Rician factor and inverse of XPD are assumed to be $K = 13$ dB and $\chi = 0.15$, respectively. In addition, an ideal analog beamforming is assumed during simulation.

The simulation is based on the OFDM model from Section II. The transmitted signal is generated by applying the pre-5G system parameters listed in Table 1 to the OFDM

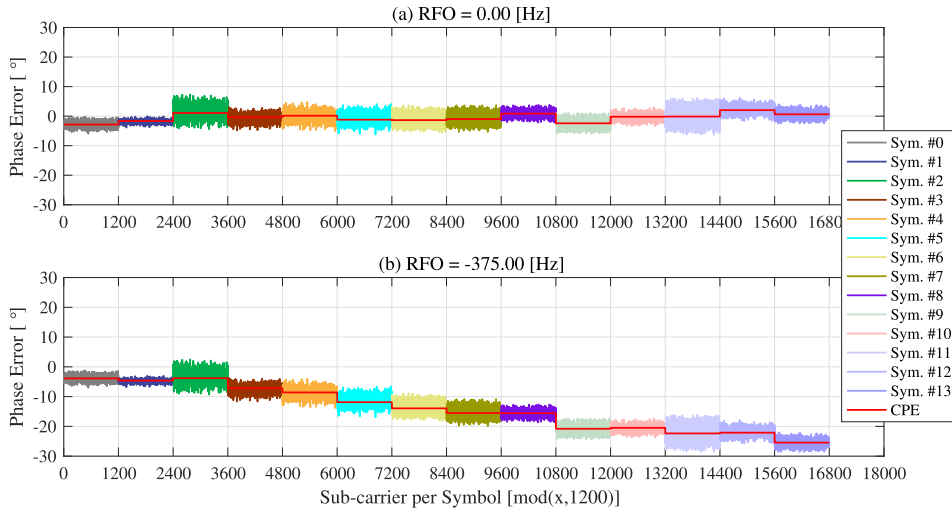


FIGURE 8. Phase error in frequency domain.

model. Then, we reflect the PN characteristics in Fig. 7 to the transmitted signal. For PN compensation on the signal, we first obtain the frequency-domain data and channel estimates by the FFT and then apply the phase error compensation method from Section III-B.

The phase error and estimated CPE in the frequency domain are shown in Fig. 8. The variation of the phase error and estimated CPE depends on the symbol, and the phase error is more severe for larger RFO. This is because the RFO effect increases with the symbol index. For example, the maximum phase error is about -30° at the last symbol when $RFO f_o = -375$ (i.e., $\epsilon = -0.005$), and the maximum phase error is 8° without RFO.

B. SIMULATION AND EXPERIMENTAL RESULTS

Here, we evaluate the RFO, phase error, and EVM performance through the simulation described in Section V-A. In Fig. 9, we investigate the accuracy of RFO in terms of mean and standard deviation (STD) when the number of accumulations for the estimated frequency offset increases at a signal-to-noise ratio (SNR) of 28 dB. Frequency offset estimation relies on the delay correlation from the SS in the TDP. Fig. 9(a) shows that the mean RFO is very robust to varying number of accumulations. In Fig. 9(b), the STD of RFO decays as the number of accumulations increases. Hence, the estimated frequency offset should be accumulated multiple times to reduce the RFO, as the PN undermines frequency offset estimation. In the implemented pre-5G system, we set the number of accumulations for the estimated frequency offset to 50, at which the STD of the simulated RFO almost converges (Fig. 9(b)). The mean and STD of the measured RFO are similar to those of the simulated RFO at 50 accumulations. However, despite the accumulations, the STD of RFO still remains at 72 Hz, resulting in a severe phase error.

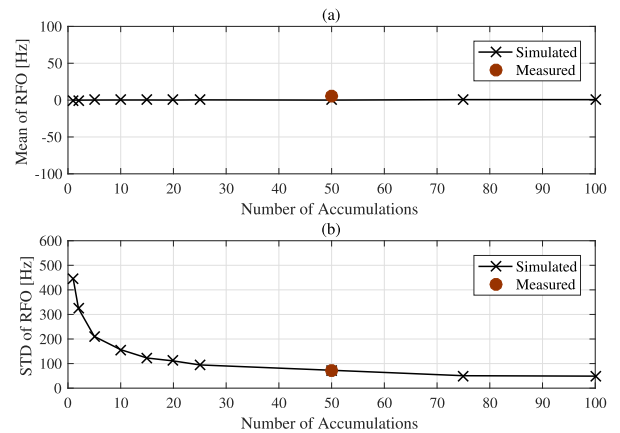


FIGURE 9. Accuracy of RFO according to number of accumulations.

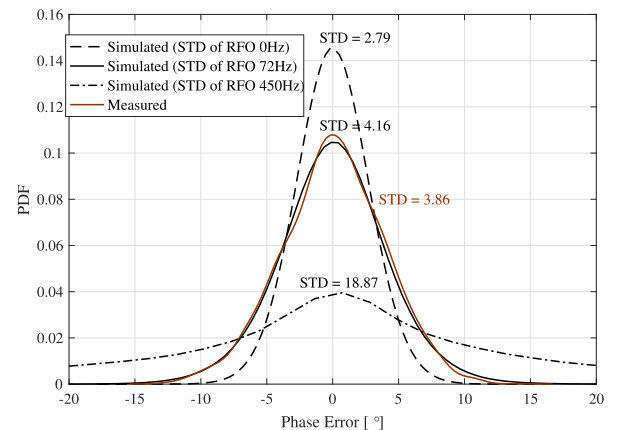


FIGURE 10. PDF of simulated and measured phase errors.

To evaluate the influence of the RFO on the phase error, Fig. 10 shows the variation of the probability density functions (PDFs) of the simulated and measured phase errors for

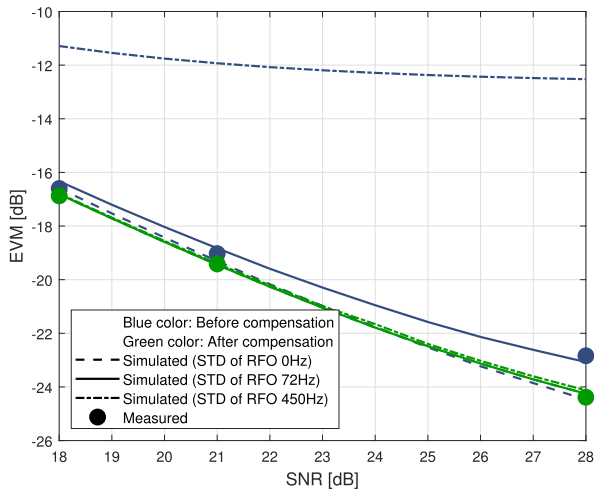


FIGURE 11. Simulated and measured EVM for different SNRs.

varying RFO STD at SNR of 28 dB. The STD of the simulated phase error is very large at 450 Hz, which corresponds to the RFO STD without accumulation. When the RFO STD reduces to 0 Hz, the STD of the phase error decreases. The STD of the measured phase error is 3.86° , being similar to that of the simulated phase error when the RFO STD is 72 Hz. Hence, the PN model suitably agrees with the real PN at a 0.3° error. In addition, when the RFO STD is zero, the STD of the simulated phase error is 2.79° , which reflects only the effect of the random phase error. As STDs of the measured and random phase errors are 3.86° and 2.79° , respectively, the effect of the random part from the measured phase error accounts for approximately 72%.

The EVM performance is illustrated in Fig. 11 for varying SNR at different RFO STDs. To examine only the PN

effect, the EVM performance before the compensation is first determined. As the phase error is more severe when the RFO accuracy decreases (see Fig. 10), the EVMs increase with the RFO STD for all SNRs. For example, at SNR of 28 dB, the simulated EVMs are -12.5 , -23.0 , and -24.4 dB for RFO STDs of 450, 72, and 0 Hz, respectively. The simulated EVM of RFO STDs of 72 Hz is similar to the measured EVM of -22.8 dB. Next, after phase error compensation, the EVM performance notably improves compared to that before compensation. The EVM performances after compensation are similar because the phase error is successfully compensated. With phase error compensation, the measured EVM improvements are higher as the SNR increases, being of 0.2, 0.3, and 1.5 dB at SNRs of 18, 21, and 28 dB, respectively.

Based on the results of EVM, its influence on throughput is also analyzed. Fig. 12 shows the distribution of the allocated modulation coding scheme (MCS) and throughput in the implemented pre-5G system. The measurements were collected for a CC with the TDD configuration shown in Fig. 2. Fig. 12(a) shows that the MCS allocation before and after phase error compensation is similar at SNRs of 18 and 21 dB. However, at 28 dB, the MCS is allocated up to 11 before compensation. In contrast, the MCS can be allocated from 12 to 14 after compensation given the EVM improvement of 1.5 dB at only 28 dB SNR (Fig. 12). Specifically, the EVM of -24.3 dB after the EVM improvement of 1.5 dB can support the MCS of 14, as the required EVM is -24 dB to support this scheme with subframe error below 10%. The MCS of 14 is defined as 64 quadrature amplitude modulation with an effective code rate of 0.8 in the pre-5G specification [7]. The higher MCS allocation is seen at SNR of 28 dB in Fig. 12(b), where the throughput of 342 Mbps before compensation increases by 149% up to 511 Mbps after compensation. Interestingly, the

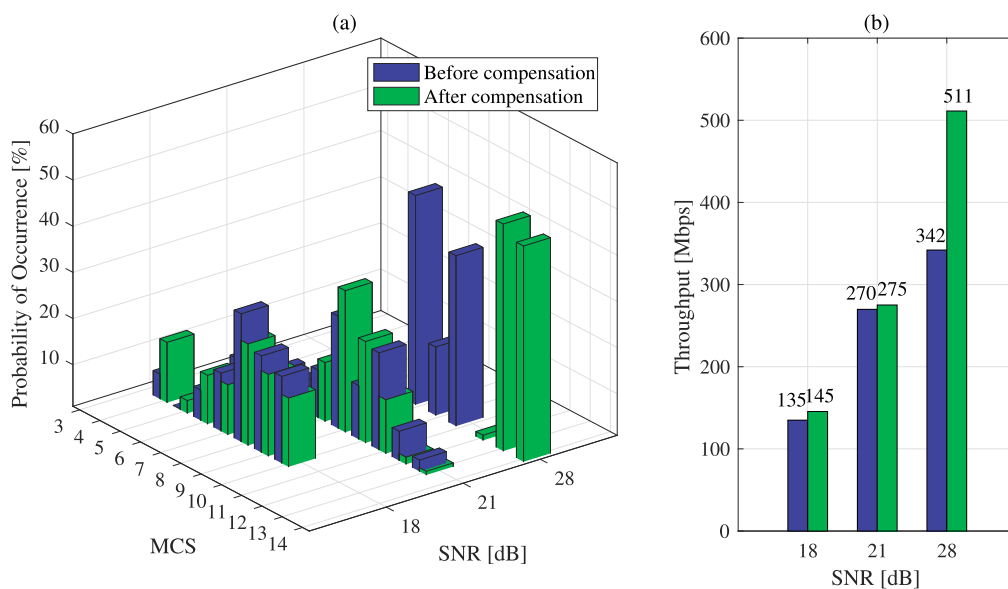


FIGURE 12. Throughput and allocated MCS distribution for different SNR.

throughput can have almost 4 Gbps with 1.352 Gbps gain if the pre-5G system is extended to eight CCs.

VI. CONCLUSION

We present a pre-5G system operating in millimeter bands and its implementation as a 5G-enabled device. To thoroughly analyze the PN effect on the pre-5G system, we describe the method and implementation of phase error compensation in the implemented system. By modeling the implemented pre-5G system, we analyze the PN effect on phase error and the system performance via simulations. Measurements of the PN effect in the implemented pre-5G system are compared with the simulation results, confirming that the simulated and measured phase errors are similar, and the throughput in the implemented pre-5G system can achieve almost 4 Gbps with a 1.49 gain from phase error compensation.

An important direction for future research is to investigate the PN effect on a large channel bandwidth. The current 5G system can support the channel bandwidth up to 400 MHz using a sub-carrier spacing of 480 KHz. In the system using the maximum channel bandwidth, the PN would differently affect the system performance according to available sub-carrier spacings. Another important extension is to measure the system performance caused by the PN at the high frequency band such as *V*- and *D*-bands. The implemented RFIC that has an affordable PN is a challenging research for those bands. Thus, it would be interesting to study a sophisticated PN compensation at the *V*- and *D*-bands.

REFERENCES

- [1] W. Roh, J.-Y. Seol, J. Park, B. Lee, J. Lee, Y. Kim, J. Cho, K. Cheun, and F. Aryanfar, "Millimeter-wave beamforming as an enabling technology for 5G cellular communications: Theoretical feasibility and prototype results," *IEEE Commun. Mag.*, vol. 52, no. 2, pp. 106–113, Feb. 2014.
- [2] Y. Kim, H.-Y. Lee, P. Hwang, R. K. Patro, J. Lee, W. Roh, and K. Cheun, "Feasibility of mobile cellular communications at millimeter wave frequency," *IEEE J. Sel. Topics Signal Process.*, vol. 10, no. 3, pp. 589–599, Apr. 2016.
- [3] R. W. Heath, Jr., N. Gonzalez-Prelcic, S. Rangan, W. Roh, and A. M. Sayeed, "An overview of signal processing techniques for millimeter wave MIMO systems," *IEEE J. Sel. Topics Signal Process.*, vol. 10, no. 3, pp. 436–453, Apr. 2016.
- [4] S. Hur, H. Yu, J. Park, W. Roh, C. U. Bas, R. Wang, and A. F. Molisch, "Feasibility of mobility for millimeter-wave systems based on channel measurements," *IEEE Commun. Mag.*, vol. 56, no. 7, pp. 56–63, Jul. 2018.
- [5] V. W. Wong, R. Schober, D. W. K. Ng, and L.-C. Wang, *Key Technologies for 5G Wireless Systems*. Cambridge, U.K.: Cambridge Univ. Press, 2017.
- [6] PyeongChang 5G Special Interest Group (5GSIG); *Technical Specification Group Radio Access Network; PyeongChang 5th Generation Radio, Physical Layer; Physical Channels and Modulation (Release 1)*, document TS 5G.211, V2.6, Sep. 2016.
- [7] Verizon 5G TF; *Air Interface Working Group; Verizon 5th Generation Radio Access; Physical Channels and Modulation (Release 1)*, document TS V5G.211, V1.8, Dec. 2016.
- [8] *Technical Specification Group Radio Access Network; NR; Base Station (BS) Radio Transmission and Reception (Release 15)*, document TS 38.104, V1.0.0, 3GPP, Dec. 2017.
- [9] S. Rangan, T. S. Rappaport, and E. Erkip, "Millimeter-wave cellular wireless networks: Potentials and challenges," *Proc. IEEE*, vol. 102, no. 3, pp. 366–385, Mar. 2014.
- [10] J. Zhang, X. Ge, Q. Li, M. Guizani, and Y. Zhang, "5G millimeter-wave antenna array: Design and challenges," *IEEE Wireless Commun.*, vol. 24, no. 2, pp. 106–112, Apr. 2017.
- [11] D. Petrovic, W. Rave, and G. Fettweis, "Effects of phase noise on OFDM systems with and without PLL: Characterization and compensation," *IEEE Trans. Commun.*, vol. 55, no. 8, pp. 1607–1616, Aug. 2007.
- [12] X. Cheng, K. Xu, and S. Li, "Compensation of phase noise in uplink massive MIMO OFDM systems," *IEEE Trans. Wireless Commun.*, vol. 18, no. 3, pp. 1764–1778, Mar. 2019.
- [13] V. S. Abhayawardhana and I. J. Wassell, "Common phase error correction with feedback for OFDM in wireless communication," in *Proc. Global Telecommun. Conf. (GLOBECOM)*, Nov. 2002, pp. 651–655.
- [14] L. Koschel and A. Kortke, "Frequency synchronization and phase offset tracking in a real-time 60-GHz CS-OFDM MIMO systems," in *Proc. IEEE PIMRC*, Sep. 2012, pp. 2281–2286.
- [15] Y. Zhang and H. Liu, "MIMO-OFDM systems in the presence of phase noise and doubly selective fading," *IEEE Trans. Veh. Technol.*, vol. 56, no. 4, pp. 2277–2285, Jul. 2007.
- [16] S. Stefanatos, F. Foukalas, and T. Khatib, "On the achievable rates of OFDM with common phase error compensation in phase noise channels," *IEEE Trans. Commun.*, vol. 65, no. 8, pp. 3509–3521, Aug. 2017.
- [17] A. Ishaque and G. Ascheid, "On the efficient mitigation of phase noise in MIMO-OFDM receivers," in *Proc. Int. Symp. Signals, Syst., Electron. (ISSSE)*, Oct. 2012, pp. 1–6.
- [18] C.-Y. Ma, C.-Y. Wu, and C.-C. Huang, "A simple ICI suppression method utilizing cyclic prefix for OFDM systems in the presence of phase noise," *IEEE Trans. Commun.*, vol. 61, no. 11, pp. 4539–4550, Nov. 2013.
- [19] S. Suyama, H. Suzuki, K. Fukawa, and J. Izumi, "Iterative receiver employing phase noise compensation and channel estimation for millimeter-wave OFDM systems," *IEEE J. Sel. Areas Commun.*, vol. 27, no. 8, pp. 1358–1366, Oct. 2009.
- [20] X. Yang, M. Matthaiou, J. Yang, C.-K. Wen, F. Gao, and S. Jin, "Hardware-constrained millimeter-wave systems for 5G: Challenges, opportunities, and solutions," *IEEE Commun. Mag.*, vol. 57, no. 1, pp. 44–50, Jan. 2019.
- [21] O. H. Salim, A. A. Nasir, H. Mehrpouyan, W. Xiang, S. Durrani, and R. A. Kennedy, "Channel, phase noise, and frequency offset in OFDM systems: Joint estimation, data detection, and hybrid Cramér-Rao lower bound," *IEEE Trans. Commun.*, vol. 62, no. 9, pp. 3311–3325, Sep. 2014.
- [22] T. A. Thomas, M. Cudak, and T. Kovarik, "Blind phase noise mitigation for a 72 GHz millimeter wave system," in *Proc. IEEE Int. Conf. Commun. (ICC)*, Jun. 2015, pp. 1352–1357.
- [23] K. Matsumoto, Y. Chang, G. K. Tran, and K. Araki, "Frequency domain phase noise compensation employing adaptive algorithms for millimeter-wave OFDM systems," in *Proc. Asia-Pacific Microw. Conf.*, 2014, pp. 1262–1264.
- [24] H. Huang, W. G. J. Wang, and J. He, "Phase noise and frequency offset compensation in high frequency MIMO-OFDM system," in *Proc. IEEE Int. Conf. Commun. (ICC)*, Jun. 2015, pp. 1280–1285.
- [25] L. Zhao, D. W. K. Ng, and J. Yuan, "Multi-user precoding and channel estimation for hybrid millimeter wave systems," *IEEE J. Sel. Areas Commun.*, vol. 35, no. 7, pp. 1576–1590, Jul. 2017.
- [26] J. Rodriguez-Fernandez and N. Gonzalez-Prelcic, "Joint synchronization, phase noise and compressive channel estimation in hybrid frequency-selective mmWave MIMO systems," 2019, *arXiv:1906.02169*. [Online]. Available: <http://arxiv.org/abs/1906.02169>
- [27] C. Kim, T. Kim, and J. Y. Seol, "Multi-beam transmission diversity with hybrid beamforming for MIMO-OFDM systems," in *Proc. IEEE GLOBECOM Workshops*, Dec. 2013, pp. 61–65.
- [28] S. Kim, J. Choi, and J. Song, "Beam designs for millimeter-wave backhaul with dual-polarized uniform planar arrays," *IEEE Trans. Commun.*, vol. 68, no. 7, pp. 4202–4217, Jul. 2020.
- [29] T. Kim, J. Park, J.-Y. Seol, S. Jeong, J. Cho, and W. Roh, "Tens of Gbps support with mmWave beamforming systems for next generation communications," in *Proc. IEEE Global Commun. Conf. (GLOBECOM)*, Dec. 2013, pp. 3685–3690.
- [30] C. Kim, J.-S. Son, T. Kim, and J.-Y. Seol, "On the hybrid beamforming with shared array antenna for mmWave MIMO-OFDM systems," in *Proc. IEEE Wireless Commun. Netw. Conf. (WCNC)*, Apr. 2014, pp. 335–340.
- [31] P. Xu, Y. Xiao, S. Zhou, and M. Zhao, "ICI analysis of MIMO-OFDM systems with independent phase noise at both transmit and receive antennas," in *Proc. 5th Int. Conf. Wireless Commun., Netw. Mobile Comput.*, Sep. 2009, pp. 1–4.
- [32] T.-J. Lee and Y.-C. Ko, "Channel estimation and data detection in the presence of phase noise in MIMO-OFDM systems with independent oscillators," *IEEE Access*, vol. 5, pp. 9647–9662, 2017.
- [33] V. Erceg, M. Messe, A. Tarighat, M. Boers, J. Trachewsky, and C. Choi, *60 GHz Impairments Modeling*, document IEEE 802.11-09/1213r1, 2009.
- [34] M. K. Samimi and T. S. Rappaport, "3-D millimeter-wave statistical channel model for 5G wireless system design," *IEEE Trans. Microw. Theory Techn.*, vol. 64, no. 7, pp. 2207–2225, Jul. 2016.



JONGHO OH (Member, IEEE) received the B.S.E., M.S.E., and Ph.D. degrees in electrical engineering from the Korea Advanced Institute of Science and Technology (KAIST), Daejeon, South Korea, in 2004, 2005, and 2011, respectively. From 2004 to 2009, he was a Teaching and Research Assistant with the Department of Electrical Engineering and Computer Science, KAIST. From 2011 to 2017, he was a Senior Engineer with Samsung Electronics Company Ltd., Suwon, South Korea. Since 2017, he has been a Principal Engineer with Samsung Electronics Company Ltd., where he has been involved in development of 5G communications systems. His research interests include large-scale MIMO systems and millimeter wave communications.



TAE-KYOUNG KIM (Member, IEEE) received the B.S. and Ph.D. degrees in electronic and electrical engineering from the Pohang University of Science and Technology (POSTECH), Pohang, South Korea, in 2009 and 2015, respectively. From 2015 to 2018, he was a Senior Researcher with Samsung Electronics Company Ltd., Suwon, South Korea, where he was involved in development of 5G modem communications systems. Since 2018, he has been an Assistant Professor with Mokpo National University, Muan, South Korea. His research interests include large-scale MIMO systems and millimeter wave communication systems.

...